An improved empirical model of electron and ion fluxes at geosynchronous orbit based on upstream solar wind conditions.

M. H. Denton[1,2], M. G. Henderson[3], V. K. Jordanova[3], M. F. Thomsen[4], J. E. Borovsky[1,5], J. Woodroffe[3], D. P. Hartley[6], and D. Pitchford[7].

1. Center for Space Plasma Physics, Space Science Institute, CO 80301, USA.

2. New Mexico Consortium, Los Alamos, NM 87544, USA.

3. ISR-1, Los Alamos National Laboratory, NM 87545, USA.

4. Planetary Science Institute, AZ 85719, USA.

5. University of Michigan, Michigan, Ann Arbor, MI 48109, USA.

6. University of Iowa, Iowa City, IA 52242, USA.

7. SES Engineering, L-6815 Château de Betzdorf, Luxembourg.

ABSTRACT

A new empirical model of the electron fluxes and ion fluxes at geosynchronous orbit (GEO) is introduced, based on observations by Los Alamos National Laboratory (LANL) satellites. The model provides flux predictions in the energy range ~1 eV to ~40 keV, as a function of local-time, energy, and the strength of the solar-wind electric field (the negative product of the solar wind speed and the z-component of the magnetic field). Given appropriate upstream solar-wind measurements, the model provides a forecast of the fluxes at GEO with a ~1 hour lead time. Model predictions are tested against in-sample observations from LANL satellites, and also against out-of-sample observations from the CEASE-II detector on the AMC-12 satellite. The model does not reproduce all structure seen in the observations. However, for the intervals studied here (quiet and storm times) the Normalized-Root-Mean-Squared-Deviation (NRMSD) <~0.3. It is intended that the model will improve forecasting of the spacecraft environment at GEO and also provide improved boundary/input conditions for physical models of the magnetosphere.

1. Introduction

Geosynchronous orbit (GEO), at a radial distance of 6.6 R_E (Earth radii), is one of the most popular locations for communications, scientific, and military satellites (see Figure 1). This is primarily due to the fact that satellites located in this orbit have an orbital period of 24 hours, allowing them to remain at the same geographic longitude above the Earth during their operational lifetime. Predictions of the plasma environment encountered by satellites at GEO [*Purvis et al.*, 1984; *O'Brien and Lemon*, 2007; *Thomsen et al.*, 2007; *Sicard-Piet et al.*, 2008; *O'Brien*, 2009; *Ginet et al.*, 2014; *Hartley et al.*, 2014; *Ganushkina et al.*, 2013; 2014; 2015; *Denton et al.*, 2015] provide spacecraft designers and operators with estimates of the plasma conditions (e.g. the ion flux and the electron flux) that satellite hardware will be subjected to on orbit. If such predictions are based on upstream solar-wind conditions (e.g. measured by the ACE satellite or the DSCOVR satellite situated in Lissajous orbits at the L1 Lagrangian point between the Earth and the Sun) then this allows a lead time of around one hour from the flux predictions being made to when such fluxes may be encountered. Since elevated fluxes are generally considered a hazard for satellites, a lead time of around one hour can be used to potentially take remedial action with the intention of mitigating damaging effects upon the satellite hardware. Understanding the environment at GEO is one scientific topic where the operational community and the scientific community both invest significant effort and where each communities priorities may be aligned [*O'Brien et al.*, 2013].

In addition to the hardware-related uses of electron and ion flux predictions, a variety of scientific models of the inner magnetosphere also use fluxes at GEO as their outer boundary conditions (e.g. *Jordanova et al.* [1998; 2003], *Zaharia et al.* [2005; 2006], *Katus et al.* [2014]). Hence, development of improved predictions of the fluxes at GEO has the potential to benefit both the scientific and

operational communities.

In a recent study we introduced a new model of the ion and electron fluxes at GEO in the energy range ~1 eV to ~40 keV as a function of local time, geomagnetic activity, and solar-activity [*Denton et al.*, 2015]. The model is based on observations made between 1989 and 2007 by seven Los Alamos National Laboratory (LANL) satellites based at GEO. Magnetospheric Plasma Analyzer (MPA) instruments (electro-static analyzers) onboard the satellites measure both the electron and the ion energy-per-charge distributions between ~1 eV/q and ~40 eV/q [*Bame et al.*, 1989; *Thomsen et al.*, 1999]. In brief, each point in the entire MPA dataset (over 80 satellite-years of data) was allocated to the appropriate bin based on an array of 40 energies (equally spaced logarithmically between 1 eV and 40 eV), 24 local-times, and 28 discrete values of the Kp index [*Bartels et al.*, 1939; *Thomsen,* 2004], for both ions and electrons. Solar activity variations were included in the model by carrying out the above binning for four ranges of the F10.7 index (all F10.7, F10.7 < 100, 100 <F10.7 < 170, and F10.7 > 170). Statistical averaging for each grid allowed the mean, median, and standard deviation for each bin to be calculated whilst bi-linear interpolation allowed flux predictions to be made for any chosen input values. The model also returned predictions of the 5th, 25th, 75th, and 95th percentiles of the flux values for any chosen combination of input values. Hence, in the published version of the original model, the user can input a particular energy, local time, and value of the Kp index, and the model will return a prediction of the electron flux and the ion flux to be encountered at GEO for the chosen energy, chosen local time, and chosen Kp index, at four different levels of solar activity [*Denton et al.*, 2015].

The bulk morphology of the electrons and ions at GEO, in the energy range sampled by LANL/MPA,

has previously been shown to be well-correlated with the level of magnetospheric convection [*Korth et al.*, 1999; *Denton et al.*, 2005; 2007; *Lavraud et al.*, 2005]. And since the Kp index, with a 3 hour cadence, is a very good proxy for this magnetospheric convection [*Thomsen*, 2004], then the original model predicted fluxes that were in reasonably good agreement with observations. However, two disadvantages arise from use of the Kp index, with particular regard to predictions. Firstly, the K index (from which Kp is derived) is an Earth-based index, constructed from magnetometer measurements of the horizontal component of the terrestrial magnetic field. Hence, estimates of flux at Earth (geosynchronous orbit), based on the Kp index, are only available on an instantaneous basis (i.e. a 'nowcast'), rather than being true advance predictions (i.e. a 'forecast'). Secondly, the fluxes at GEO are regularly observed to fluctuate much more rapidly than three-hour time cadence of the Kp index, typically in response to dynamic changes in the solar wind with timescales much less than one hour in duration. Thus, our desire for a new and improved predictive model is driven by the following criteria: (i) that the new model should be driven by some set of parameters that are regularly measured in the solar wind, upstream of the Earth, and thus provide at least a one-hour time interval between prediction of the fluxes and arrival of the fluxes at GEO, (ii) that the activity parameters should be capable of a time cadence of at least one hour, and preferably as short as one minute, and (iii) that the new model produce flux predictions that are, in the majority of cases, comparable with, or better than, the previous version of the model. As outlined below, the results summarized in this study indicate that we have largely achieved our intended aims by parameterizing the new model with the measured value of the solar-wind electric field at the L1 point. The developmental methodology used in formulating the new model is outlined in detail in Section 2, comparisons between model predictions and in-situ observations of fluxes are made, along with goodness-of-fit calculations, in Section 3, and a discussion of the strengths and weaknesses of the current model, and a summary, are provided in Section 4.

2. Model Methodology

The methodology followed in generating a new model of the fluxes at GEO is very similar to that used in the previous model, and described in detail in *Denton et al.* [2015]. The dataset for the model comprises ~82 satellite-years of electron and ion observations made between 1989 and 2007 by the LANL/MPA instruments flown on seven satellites at GEO. All flux measurements during this period are utilized when concurrent solar-wind measurements are available in the OMNI2 database [*King and Papitashvili*, 2005]. Periods when individual satellites are outside the magnetopause (usually during extremely high solar-wind pressure events) are excluded from the binning. One difference between this study and the previous *Denton et al.* [2015] study is that here we do not remove periods of exceptionally high spacecraft surface charging. The methodology to correct the particle energies resulting from the charging (due to acceleration towards the spacecraft, or repulsion away from the spacecraft), is considered robust [*Thomsen et al.*, 1999].

In brief, all available flux values (for electrons and ions) are binned into one-hour width bins in local time, 40 logarithmically spaced bins in energy (from 1 eV to 40 keV), and 32 equal-width bins in $-v_{sw}B_z$ (from -8000 to +8000 $\mu V\ m^{-1}$). This binning yields a set of three-dimensional data-cubes that contain the mean, standard-deviation, and the 5^{th}, 25^{th}, 50^{th}, 75^{th}, and 95^{th} percentiles of all data contributing to each bin (see Figure 3). In order to provide the average conditions at any local-time, energy or $-v_{sw}B_z$, bi-linear interpolation (with respect to the chosen local time and energy) and linear interpolation (with respect to $-v_{sw}B_z$) is used. The local time (in hours), the energy (in eV), and the negative product of the solar wind flow speed (v_{sw} in units of km s^{-1}) and the z-component of the solar-wind magnetic field (B_z in GSM coordinates in units of nT), are chosen by the user. This product is

122 the solar-wind electric field ($-v_{sw} \times B_z$) in units of $\mu V\ m^{-1}$ and in this parameterization, a solar wind
123 speed of 450 km s^{-1} in a magnetic field value of B_z = -14.7 nT (GSM) yields an electric field of +6615
124 $\mu V\ m^{-1}$. It is generally accepted that, as with the Kp index, the solar-wind electric field is reasonably
125 well-correlated with activity in the magnetosphere, although the detailed micro-physics that control the
126 coupling are beyond the scope of this paper (see *Newell et al.* [2007]; *Borovsky* [2013; 2014];
127 *McPherron et al.* [2015] for further discussions on this topic).
128
129 Although it is planned to evaluate more advanced coupling functions in future, use of the $-v_{sw}B_z$
130 parameter has the advantage of being well-known in the science and operational community, easily
131 computed, and widely available over the duration of the LANL/MPA dataset. In addition, this
132 parameter will be available in future via the continued operation of the ACE and DSCOVR satellites.
133 Solar wind data, propagated to the magnetopause, are taken from the high-resolution OMNI2 database
134 [*King and Papitashvili*, 2005] and MPA flux values are only included in the binning if solar-wind data
135 are available at the time of each data-point. To ensure a sufficient amount of data in each bin we have
136 limited the binning to $-v_{sw}B_z$ values between -8000 and +8000 $\mu V\ m^{-1}$, and do not provide separate
137 predictions for different values of the F10.7 index. [Note: The maximum flux variation between solar
138 maximum and solar minimum in the previous model was around a factor of 2, and only that large for a
139 small range of energies (~few keV). It is envisaged that users who will have a particular interest in
140 solar cycle effects will be able to examine the F10.7 variations in the previous model to gain insight
141 into the expected small changes with F10.7 in the new model].
142
143 The mean, standard-deviation, and the 5^{th}, 25^{th}, 50^{th}, 75^{th}, and 95^{th} percentiles in each bin are calculated
144 for ions and electrons. Figure 2 contains a schematic representation of the binning process and Figure

3 shows the results of this binning for the mean electron flux, and the mean ion flux, at two example energies. The plots in this figure demonstrate how differences in the orientation of the interplanetary magnetic field direction (IMF), either northwards or southwards, radically change the average measured flux at GEO for both the electrons and the ions. Clearly, such differences are neglected when only considering the overall level of convection (proxied by Kp) as is the case in our previous model [*Denton et al.*, 2015]. Thus, we expect an increase in the prediction accuracy of the new model as a result. Figure 4 contains example surface plots showing the electron and ion flux variability, as a function of energy and local-time, for the one particular case when $-v_{sw}B_z = -2000\ \mu V\ m^{-1}$.

3. Comparison of Model Predictions with Observations

In comparing observations with model predictions the aim is to evaluate both the general level of prediction ability of the model (goodness-of-fit), and also the incident solar-wind conditions for which the model predictions may be more, or less, accurate. Here, model predictions are compared against two different sets of observations - those provided by the LANL/MPA instruments themselves and those from the independent CEASE-II instrument [*Dichter et al.*, 1998] onboard the AMC-12 satellite, also located at GEO. The root-mean-squared deviation (RMSD) and the normalized root-mean-squared deviation (NRMSD) between the measured fluxes and the model predictions are calculated via the equation

$$\mathrm{NRMSD} = \mathrm{RMSD} \,/(\overline{x}) = \sqrt{\frac{\sum_{x=1}^{n}\left[\left(x_{i,\,\mathrm{model}} - x_{i,\,\mathrm{measured}}\right)^2\right]}{n}} \Big/ (\overline{x}) \qquad (1)$$

where n is the number of data points over the range of the comparison and $\overline{x}$ is the mean value of x over this range. Both NRMSD and RMSD are calculated in order to provide metrics with which to quantify the model accuracy (cf. *Legates and McCabe Jr.*, 1999; *Ganushkina et al.*, 2015) although a

wide spectrum of other metrics may be used when comparing models to data [*Koh et al.*, 2012], each with particular strengths and weaknesses. There are no universally accepted metrics for what represents a 'good' NRMSD value, and certainly the calculated NRMSD values depend heavily on the interval being studied. However, small values represent a better match between observations and predictions than large values. The special case of RMSD=0 (NRMSD=0) would represent a perfect forecast of the variation in the time-series being evaluated.

3.1 Comparison with LANL/MPA observations

A comparison of model predictions with the LANL/MPA observations at GEO is made for a calm five-day period during 2004. Figure 5 contains electron observations and ion observations (at energies ~32 keV) from the LANL-02A satellite (solid black line) along with model predictions from the Kp version of the model (left column) and the new model driven by the solar wind electric field, $-v_{sw}B_z$ (right column). Although the original aim was to provide a model with a much higher temporal resolution than the Kp model, on implementation it was found that rapid fluctuations in the $-v_{sw}B_z$ parameter resulted in rapid oscillations in model predictions. These do not accurately represent the actual observations at GEO. Although it is unclear on what timescale the bulk magnetosphere responds to changing solar-wind electric fields (likely a complicated function of particle energy, species, time-history of the system, etc.), here the model results are smoothed with a five-minute box-car average (this can be changed as required by the user) so as to smooth the oscillations in one-minute high-resolution OMNI model input data. Note: the Kp model is naturally smoothed due to the 3-hour cadence of the Kp index. The solid red line in Figure 5 is the predicted mean flux from the model, and the solid purple line is the median. The 5th, 25th, 75th and 95th percentiles are indicated by the dashed and dotted purple lines (the standard deviation is not shown). The Kp index and the $-v_{sw}B_z$ parameter

are plotted in the bottom row. The RMSD and NRMSD values for the model-data comparisons are also provided in the top right of each plot. Both versions of the model provide a reasonably good fit to the data with NRMSD values between ~0.14-0.25. Little difference is apparent between the models during these calm conditions, with the observed flux almost always falling within the 5th-to-95th percentile range of the model predictions.

The plots shown in Figure 6 follow the same format but this time for ions and electrons with energies ~10 keV) during a highly dynamic and disturbed period, also in 2004. The model predictions closely follow the trend of the observations and for this period, even during some of the most dynamic changes in the Kp index, and in $-v_{sw}B_z$. The NRMSD values are between ~0.15-0.21 for the new $-v_{sw}B_z$ model and the original Kp model at these times, and these values are typical of a range of other energies between ~1-40000 eV. Of course the $-v_{sw}B_z$ model also has the distinct advantage that it can make flux-predictions ~1 hour prior to the event, provided the upstream solar-wind electric field value is known. Again, the observed fluxes fall within the 5th-to-95th percentile range predicted by both models during almost the entire period under study, although the sharp drop in the ion flux at the start of day 94 is not predicted by either model.

A complete comparison of flux-predictions from the two different models at all observed energies can be made examining energy-time spectrograms of flux values from in-situ observations, along with simulated spectra from model predictions. Figure 7 contains electron (left column) and ion (right column) flux spectrograms from the LANL-02A satellite (top row) with simulated spectra from the Kp model (middle row) and the new $-v_{sw}B_z$ model (bottom row). The model spectra show the mean-flux predictions from each model (although it is straight-forward to also evaluate the 5th, 25th 50th, 75th or

95th percentiles flux-predictions, along with the standard deviation). The orange dashed line indicates local noon and the black dashed line indicates local midnight. Note: the observations of electron fluxes below ~100 eV should be treated with caution due to the possible presence of photoelectrons and secondary electrons contaminating the observations at these energies (see Fig. 7 top left panel).

Both the $-v_{sw}B_z$ and the Kp model flux spectra show many similarities to the observed LANL-02A spectra with the model flux values being broadly comparable to the observations. However, it is clear that there are significant differences at most energies. With respect to the electrons, the high fluxes observed at energies up to 10 keV by LANL-02A after ~15 UT are not fully captured by either model. The Kp model reproduces elevated fluxes at this time but their spatial structure is clearly affected by the three-hour cadence of the Kp index. The $-v_{sw}B_z$ model reproduces rapid fluctuations in the fluxes that result from changes in the solar-wind electric field, but in general these are not seen in the observations prior to 15 UT. With respect to the ions, both the Kp and the $-v_{sw}B_z$ model reproduce the appearance of a low-energy population (the ion plasmasphere) observed by LANL-02A but the model fluxes are somewhat lower than actually observed.

3.2 Comparison with independent AMC-12/CEASE-II observations

As in evaluation of the previous model, in order to provide independent testing of the model veracity (at least for the electron observations) we carry out a comparison of model predictions with electron flux observations from the CEASE-II sensor onboard the AMC-12 satellite at GEO. This comparison is made for DOY 180 during 2013, a particularly disturbed period during a geomagnetic storm where Kp reached a maximum ~6 and the Dst index reached a maximum excursion ~-100 at the start of the day. As was previously noted [*Denton et al.*, 2015] there is a semi-constant offset between CEASE-II

fluxes and MPA model predictions and hence to account for this difference we multiply the CEASE-II fluxes by a factor of ~15 at all times. Since no cross-calibration between the MPA and CEASE-II instruments took place prior to launch, this adjustment is akin to on-orbit cross-calibration of the fluxes. Note: for future comparison of model fluxes with measured fluxes from different satellites it would be necessary to evaluate the need for use of an appropriate cross-calibration factor.

Figure 8 shows electron fluxes measured by the CEASE-II instrument during a 24-hour period in color-spectrogram format, as a function of energy and time (top plot), along with the model electron flux predictions from the Kp model (middle panel) and the new $-v_{sw}B_z$ model (bottom panel). The Kp index and $-v_{sw}B_z$ are also shown, demonstrating the activity levels during this day The predictions from each model demonstrate that the broad features observed at GEO by out-of-sample instruments such as CEASE-II, can be predicted, even during highly disturbed periods. The advantage of the $-v_{sw}B_z$ model is that the fluxes to be encountered by the AMC-12 satellite can be predicted ~1 hour in advance, given upstream solar wind measurements of the speed and z-component of the magnetic field.

3.3 Spacecraft surface charging on LANL/MPA

Along with the electron and ion fluxes, the MPA instruments also measure the electrostatic surface potential on the LANL spacecraft, relative to the ambient plasma [*Thomsen et al.*, 1999]. Depending on their individual design and construction details, spacecraft can charge positive or negative [*DeForest*, 1972; *Garrett*, 1981; *Farthing et al.*, 1982; *Lanzerotti et al.* 1998; *Thomsen et al.* 2013]. In the case of the LANL satellites, the greatest level of charging occurs during hours of eclipse when the surface potential can reach 1000s Volts (negative) with respect to the ambient plasma. Such elevated charging can be detected by the observation of an ion-line in the ion flux measurements. This occurs

due to positive particles that are accelerated towards the spacecraft by the negative charge on the spacecraft. An example of such an ion-line can be seen between ~18-22 UT in the ion flux observations in Figure 7.

Since the MPA instruments regularly measure the spacecraft charging, it is straight-forward to extend the current flux model to include predictions of spacecraft charging, via similar methodology as that used for the fluxes. Although each spacecraft charges differently depending on its construction, the environmental conditions that give rise to dangerous levels of surface charging on one satellite are likely to pose a danger to other satellites passing through the region. Figure 9 shows the mean measured (negative) surface potential from all seven LANL satellites, in the same format as that used to calculate the flux distributions (as a function of $-v_{sw}B_z$) shown in Figure 3. It is clear from Figure 9 that the most severe surface charging of the LANL satellites occurs during southwards IMF-B_z and at spatial locations around local midnight. Charging is greatly reduced during periods of positive IMF-B_z. (cf. plots of spacecraft charging from LANL/MPA as a function of Kp, Dst, and v_{sw} given in *Denton and Borovsky* [2012]). The model predicts the level of surface charging on the LANL satellites by carrying out a bi-linear interpolation between the mean surface charging levels in the appropriate bins in Figure 9, based on the prevailing solar-wind conditions and the satellite local time. In this respect the model predictions of surface charging are calculated similarly to the model fluxes. It is planned that this predictive capability of model will be further developed in future versions.

4. Discussion and Summary

The ultimate goal of much "space weather" research is to *accurately* predict the conditions to be encountered by orbital hardware systems as far in advance as possible. Of course, it is nigh-on

impossible for 100% accurate predictions to ever be achieved. However, by carrying out the work outlined above, we aimed to achieve quantitative predictions that allow hardware operators and scientific modelers the ability to predict fluxes in advance given knowledge of upstream solar wind parameters. The absolute flux values (Figures 5 and 6), and the flux spectra (Figures 7 and 8), show that the $-v_{sw}B_z$ model provides reasonably accurate flux predictions at GEO ~1 hour in advance, providing knowledge of the solar wind electric field (e.g. from the ACE or DSCOVR satellites) is available. Such knowledge is available in real-time (e.g. from the Space Weather Prediction Center (http://www.swpc.noaa.gov/).

With a view to potential changes that could improve future flux forecasts, it is important to be guided by knowledge of the physics of the inner magnetosphere. The current model, and the previous version, considered neither the time-history of the magnetosphere at the time of the predictions, or the explicit transport times for plasma to migrate from the solar wind to the various locations around GEO. Drift times are energy dependent, and also dependent on the local convection strength. Such potentially non-linear effects can be estimated but are not known without complex particle tracing calculations. *Denton and Borovsky* [2009] estimated transport timescales from the solar wind to various locations around GEO with timescales being of the order of 0 h to 17.5 h. In addition, *Lavraud et al.* [2006] demonstrated the importance of the time-history of the system with respect to plasma conditions at GEO by examining the build up of cold, dense plasma during extended periods of northwards IMF. Our aim is to explore inclusion of both of these effects in future versions of the model.

With regard to operational uses of the model, *Thomsen et al.* [2013] demonstrated that satellite surface charging is strongly correlated with periods when the electron flux at energies between 5-10 keV

exceeds a particular threshold. That study found that satellite surface charging was most likely to occur during intervals when the electron flux at 8 keV exceeded a flux threshold of 1.4×10^{3} cm^{-2} s^{-1} str^{-1} eV^{-1}. Armed with this knowledge, one possible use of the model would be to: (i) determine appropriate cross-calibration factors between the model (based on MPA) and fluxes measured by the chosen satellite; (ii) use upstream values of solar-wind electric field to search for intervals when the predicted electron fluxes at 8 keV exceeded a flux threshold; (iii) expect elevated surface charging to be more likely during such intervals.

The model provides good agreement with in-sample MPA observations and (with appropriate on-orbit cross-calibration) with independent out-of-sample observations from the CEASE-II detector onboard AMC-12. It is hoped that the model will prove useful to the community of orbital hardware designers and satellite operators, as well as to the scientific community who use fluxes at GEO as inputs to physical models.

In summary:

1. A new model of the electron fluxes and ion fluxes at GEO, which uses the solar-wind electric field as input, has been developed. The model provides a ~1 hour advanced forecast of the fluxes at GEO in the energy range ~1 eV to ~ 40 keV.

2. The model provides forecasts of the fluxes at GEO that are comparable in accuracy to the previous model, driven by the Kp index. The main benefit from the new model is the ability to predict the fluxes in advance.

3. The model results are robust, during both quiet times and highly disturbed storm-times, as measured by the Root-Mean-Squared-Deviation (RMSD) and the Normalized Root-Mean-Squared Deviation (NRMSD). Observed fluxes are found to almost always fall between the 5th and 95th percentiles of the model predictions.

4. A new forecasting capability for spacecraft surface charging on the LANL satellites is introduced. Further development of this capability is planned for the future.

The model is freely available to users under the GNU General Public License v3.0 by contacting the author directly or via the model webpage at http://gemelli.spacescience.org/mdenton/.

Acknowledgements

The authors gratefully acknowledge the OMNI database for the solar wind and geophysical parameters used in this study. We also acknowledge use of the list of satellites at GEO maintained by Eric Johnston at www.satsig.net. This work was partially supported by the Space Hazards Induced near Earth by Large, Dynamic Storms (SHIELDS) project, funded by the U.S. Department of Energy through the LANL/LDRD Program under contract DE-AC52-06NA25396. MHD wishes to thank J. Denton for help with the Kp version of the model and comments on the current manuscript. MPA data are available by contacting the PI, Mike Henderson, at mghenderson@lanl.gov. The model, written in FORTRAN, is available from MHD at mdenton@spacescience.org, or via download at http://gemelli.spacescience.org/mdenton/ .

References

Bame, S. J., D. J. McComas, M. F. Thomsen, B. L. Barraclough, R. C. Elphic, J. P. Glore, J. C. Chavez, E. P. Evans and F. J. Wymer, Rev. Sci. Instrum., 64, 1026-1033, 1993.

Bartels, J., N. A. H. Heck, and H. F. Johnstone, The three-hour-range index measuring geomagnetic activity, J. Geophys. Res., 44, 411-454, 1939.

Borovsky, J. E., Physical improvements to the solar wind reconnection control function for the Earth's magnetosphere, J. Geophys. Res. Space Physics, 118, 2113–2121, 2013.

Borovsky, J. E., Canonical correlation analysis of the combined solar wind and geomagnetic index data sets, J. Geophys. Res. Space Physics, 119, 5364–5381, 2014.

DeForest, S. E., Spacecraft charging at synchronous orbit, J. Geophys. Res., 77, 651-659, 1972.

Denton, M. H., M. F. Thomsen, V. K. Jordanova, M. G. Henderson, J. E. Borovsky, J. S. Denton, D. Pitchford, and D. P. Hartley, An empirical model of electron and ion fluxes derived from observations at geosynchronous orbit, Space Weather, 13, 2015.

Denton, M. H., and J. E. Borovsky, Magnetosphere response to high-speed solar-wind streams: A comparison of weak and strong driving and the importance of extended periods of fast solar wind, J. Geophys. Res., 117, A00L05, doi:10.1029/2011JA017124, 2012.

Denton, M. H., and J. E. Borovksy, The superdense plasma sheet in the magnetosphere during high-speed-stream-driven storms: Plasma transport timescalesJ. Atmos. Sol-Terr. Phys, 71, 1045-1058, 2009

Denton, M. H., M. F. Thomsen, B. Lavraud, M. G. Henderson, R. M. Skoug, H. O. Funsten, J.-M. Jahn, C. J. Pollock, and J. M. Weygand, Transport of plasma sheet material to the inner magnetosphere, Geophys. Res. Lett., 34, L04105, doi:10.1029/2006GL027886, 2007.

Denton, M. H., M. F. Thomsen, H. Korth, S. Lynch, J. C. Zhang and M. W. Liemohn, Bulk plasma

properties at geosynchronous orbit, J. Geophys. Res., 110, A07223, 2005.

Dichter, B. K., J. 0. McGarity, M. R. Oberhardt, V. T. Jordanov, D. J. Sperry, A. C. Huber, J. A. Pantazis, E. G. Mullen, G. Ginet, and M. S. Gussenhoven, Compact Environmental Anomaly Sensor (CEASE): A novel spacecraft instrument for in situ measurements of environmental conditions, IEEE Trans. Nucl. Sci., 45, 2758–2764, 1998.

Farthing, W. H., J. P. Brown, and W. C. Bryant, Differential spacecraft charging on the geostationary operational satellites, NASA Tech. Memo, NASA TM-83908, 1982.

Ganushkina, N. Y., O. A. Amariutei, D. Welling, and D. Heynderickx, Nowcast model for low-energy electrons in the inner magnetosphere, Space Weather, 13, 16–34, doi:10.1002/2014SW001098, 2015.

Ganushkina, N. Y., M. W. Liemohn, O. A. Amariutei, and D. Pitchford, Low-energy electrons (5–50 keV) in the inner magnetosphere, J. Geophys. Res. Space Physics, 119, 246–259, doi:10.1002/2013JA019304, 2014.

Ganushkina, N. Y., O. Amariutei, Y. Y. Shpritz, and M. Liemohn, Transport of the plasma sheet electrons to the geostationary distances, J. Geophys. Res. Space Physics, 118, 82–98, doi:10.1029/2012JA017923, 2013.

Garrett, H. B., The charging of spacecraft surfaces, Rev. Geophys., 19, 577-616, 1981.

Ginet, G. P., T. P. O'Brien, S. L. Huston, W. R. Johnston, T. B. Guild, R. Friedel, C. D. Lindstrom, C. J. Roth, P. Whelan, R. A. Quinn, D. Madden, S. Morley, and Yi-Jiun Su, AE9, AP9 and SPM: New Models for Specifying the Trapped Energetic Particle and Space Plasma Environment, in The Van Allen Probes mission, eds N. Fox and J. L. Burch, Springer, doi:10.1007/978-1-4899-7433-4, ISBN: 978-1-4899-7432-7, 2014.

Hartley, D. P., M. H. Denton, and J. V. Rodriguez, Electron number density, temperature, and energy

density at GEO and links to the solar wind: A simple predictive capability, J. Geophys. Res. Space Physics, 119, 4556–4571, doi:10.1002/2014JA019779, 2014.

Jordanova, V. K., C. J. Farrugia, L. Janoo, J. M. Quinn, R. B. Torbert, K. W. Ogilvie, R. P. Lepping, J. T. Steinberg, D. J. McComas, and R. D. Belian, October 1995 magnetic cloud and accompanying storm activity: Ring current evolution, J. Geophys. Res., 103, 79, 1998.

Jordanova, V. K., L. M. Kistler, M. F. Thomsen, and C. G. Mouikis, Effects of plasma sheet variability on the fast initial ring current decay, Geophys. Res. Lett., 30(6), 1311, doi:10.1029/2002GL016576, 2003.

Katus, R. M., M. W. Liemohn, E. L. Ionides, R. Ilie, D. Welling, and L. K. Sarno-Smith, Statistical analysis of the geomagnetic response to different solar wind drivers and the dependence on storm intensity, J. Geophys. Res., doi:10.1002/2014JA020712, 2014.

King, J. H., and N. E. Papitashvili, Solar wind spatial scales in and comparisons of hourly Wind and ACE plasma and magnetic field data, J. Geophys. Res., 110, A02104, 2005.

Koh, T.-Y. S. Wang, and B. C. Bhatt, A diagnostic suite to assess NWP performance, J. Geophys. Res., 2012, 117, D13109, 2012.

Korth, H., M. F. Thomsen, J. E. Borovsky, and D. J. McComas, Plasma sheet access to geosynchronous orbit, J. Geophys. Res., 104, 25,047–25,061, 1999.

Lanzerotti, L. J., C. Breglia, D. W. Maurer, G. K. Johnson III, and C. G. MacLennan, Studies of spacecraft charging on a geosynchronous telecommunications satellite, Adv. Space Res., 22, 79-82, 1998.

Lavraud, B., M. F. Thomsen, J. E. Borovsky, M. H. Denton, and T. I. Pulkkinen, Magnetosphere preconditioning under northward IMF: Evidence from the study of coronal mass ejection and corotating interaction region geoeffectiveness, J. Geophys. Res., 111, A09208,

doi:10.1029/2005JA011566, 2006.

Lavraud, B., M. H. Denton, M. F. Thomsen, J. E. Borovsky, and R. H. W. Friedel, Superposed epoch analysis of dense plasma access to geosynchronous orbit, Ann. Geophys., 23, 2519–2529, 2005.

Legates, D. R., and G. J. McCabe Jr., Evaluating the use of "goodness-of-fit" Measures in hydrologic and hydroclimatic model validation, Water Resour. Res., 35(1), 233–241, doi:10.1029/1998WR900018, 1999.

McPherron, R. L., T.-S. Hsu, and X. Chu, An optimum solar wind coupling function for the AL index. J. Geophys. Res. Space Physics, 120, 2494–2515, doi: 10.1002/2014JA020619, 2015.

Newell, P. T., T. Sotirelis, K. Liou, C.-I. Meng, and F. J. Rich, A nearly universal solar wind-magnetosphere coupling function inferred from 10 magnetospheric state variables, J. Geophys. Res., 112, A01206, doi:10.1029/2006JA012015, 2007.

O'Brien, T. P., J. E. Mazur, and J. F. Fennell, The Priority Mismatch Between Space Science and Satellite Operations, Space Weather, 11, doi:10.1002/swe.20028, 2013

O'Brien, T. P., SEAES-GEO: A spacecraft environmental anomalies expert system for geosynchronous orbit, Space Weather, 7, S09003, 2009.

O'Brien, T. P., and C. L. Lemon, Reanalysis of plasma measurements at geosynchronous orbit, Space Weather, 5, S03007, doi:10.1029/2006SW000279, 2007.

Purvis, C. K., H. B. Garrett, A. C. Whittlesey, and N. J. Stevens, Design guidelines for assessing and controlling spacecraft charging effects, NASA Tech. Pap. 2361, 1984.

Sicard-Piet, A., S. Bourdarie, D. Boscher, R. H. W. Friedel, M. Thomsen, T. Goka, H. Matsumoto, and H. Koshiishi, A new international geostationary electron model: IGE-2006, from 1 keV to 5.2 MeV, Space Weather, 6, S07003, doi:10.1029/2007SW000368, 2008.

Thomsen, M. F., M. G. Henderson, and V. K. Jordanova, Statistical properties of the surface-charging

environment at geosynchronous orbit, Space Weather, 11, 237-244, 2013.

Thomsen, M. F., E. Noveroske, J. E. Borovsky, and D. J. McComas, Calculating the Moments from Measurements by the Los Alamos Magnetospheric Plasma Analyzer, LA-13566-MS, Los Alamos National Laboratory, 1999.

Thomsen, M. F., Why Kp is such a good measure of magnetospheric convection, Space Weather, 2, S11004, doi:10.1029/2004SW000089, 2004.

Thomsen, M. F., M. H. Denton, B. Lavraud, and M. Bodeau, Statistics of plasma fluxes at geosynchronous orbit over more than a full solar cycle, Space Weather, 5, S03004, doi:10.1029/2006SW000257, 2007.

Zaharia, S., M. F. Thomsen, J. Birn, M. H. Denton, V. K. Jordanova, and C. Z. Cheng, Effect of storm-time plasma pressure on the magnetic field in the inner magnetosphere, Geophys. Res. Lett., 32, L03102, doi:10.1029/2004GL021491, 2005.

Zaharia, S., V. K. Jordanova, M. F. Thomsen, and G. D. Reeves, Self-consistent modeling of magnetic fields and plasmas in the inner magnetosphere: Application to a geomagnetic storm, J. Geophys. Res., 111, A11S14, doi:10.1029/2006JA011619, 2006.

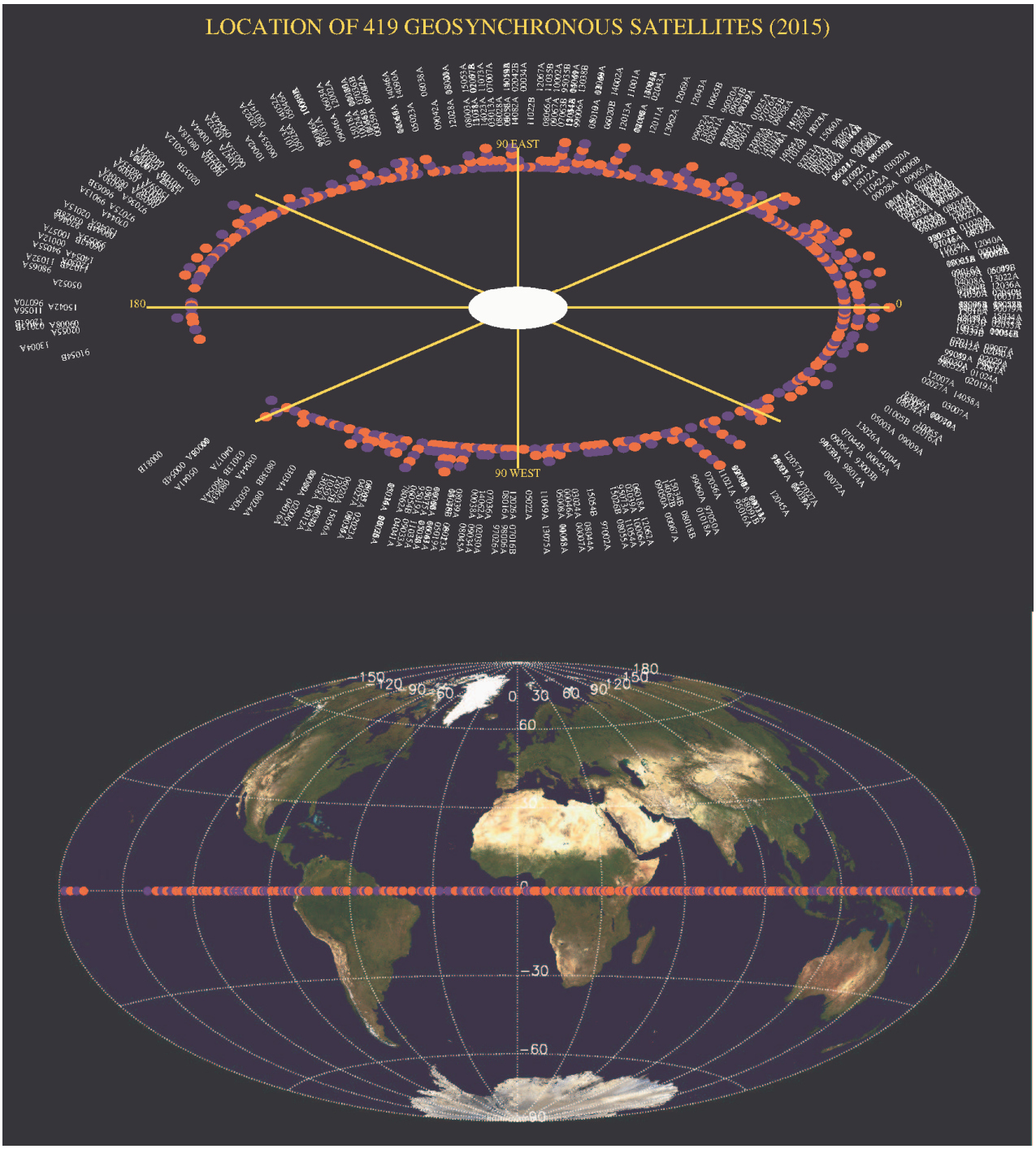

Figure 1. (Top panel) The geographic (equatorial) locations of selected Earth-orbiting satellites located in a synchronous orbit east and west of the Greenwich meridian (0° longitude). Where more than one satellite is located at the same longitude (to 0.1 degree accuracy) the satellites are displayed radially outwards from GEO. (Bottom panel) The geographic equatorial footprint of the satellites on the Earth (Hammer-Aitoff projection). Note: no account is taken of the satellite inclination. Adjacent satellites are alternately displayed in red/blue for clarity.

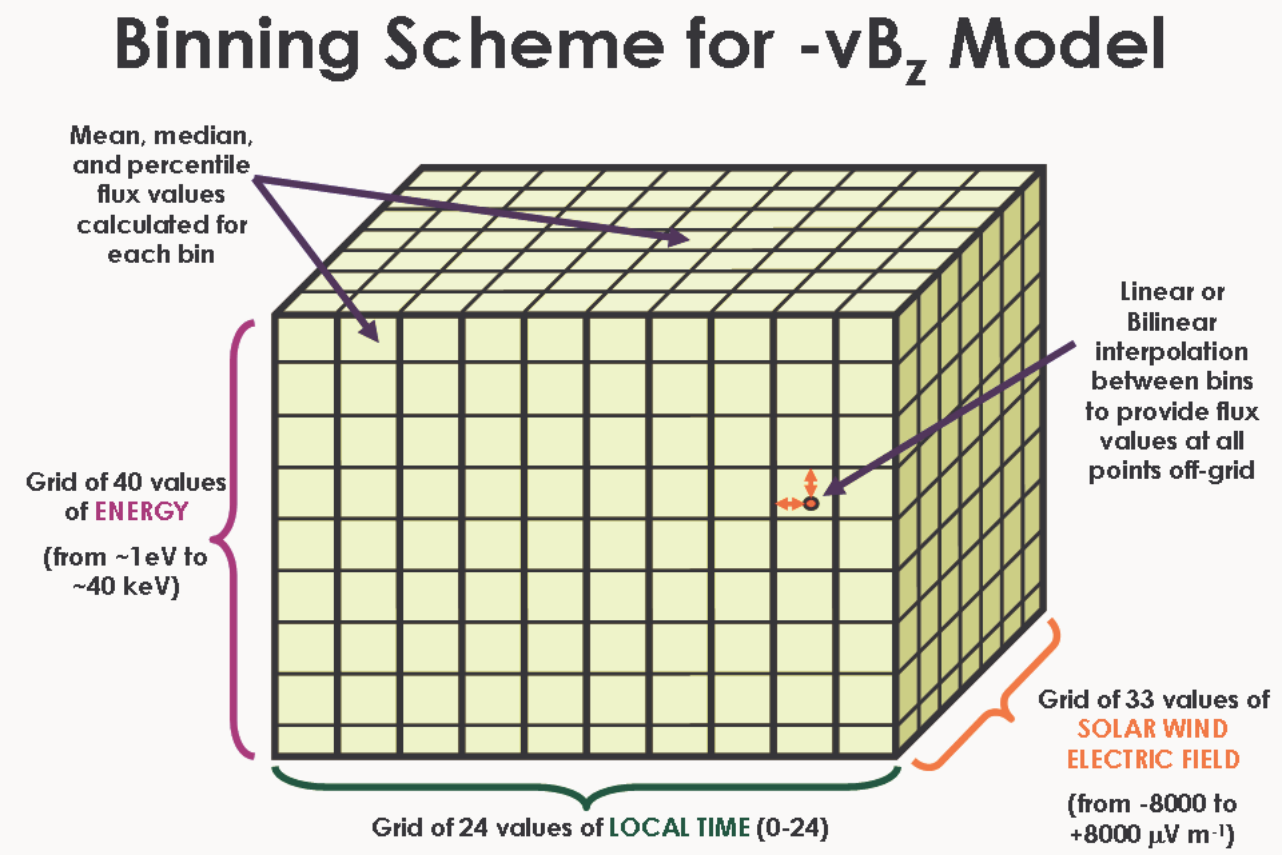

Figure 2. Schematic showing the binning scheme for the -vB_z model. The three-dimensional model grid contains 40 energy bins (between 1 eV and 40 keV), 33 bins of -vB_z values (-8000 to +8000), and 24 bins of local time (0-24), for both the ions and the electrons.

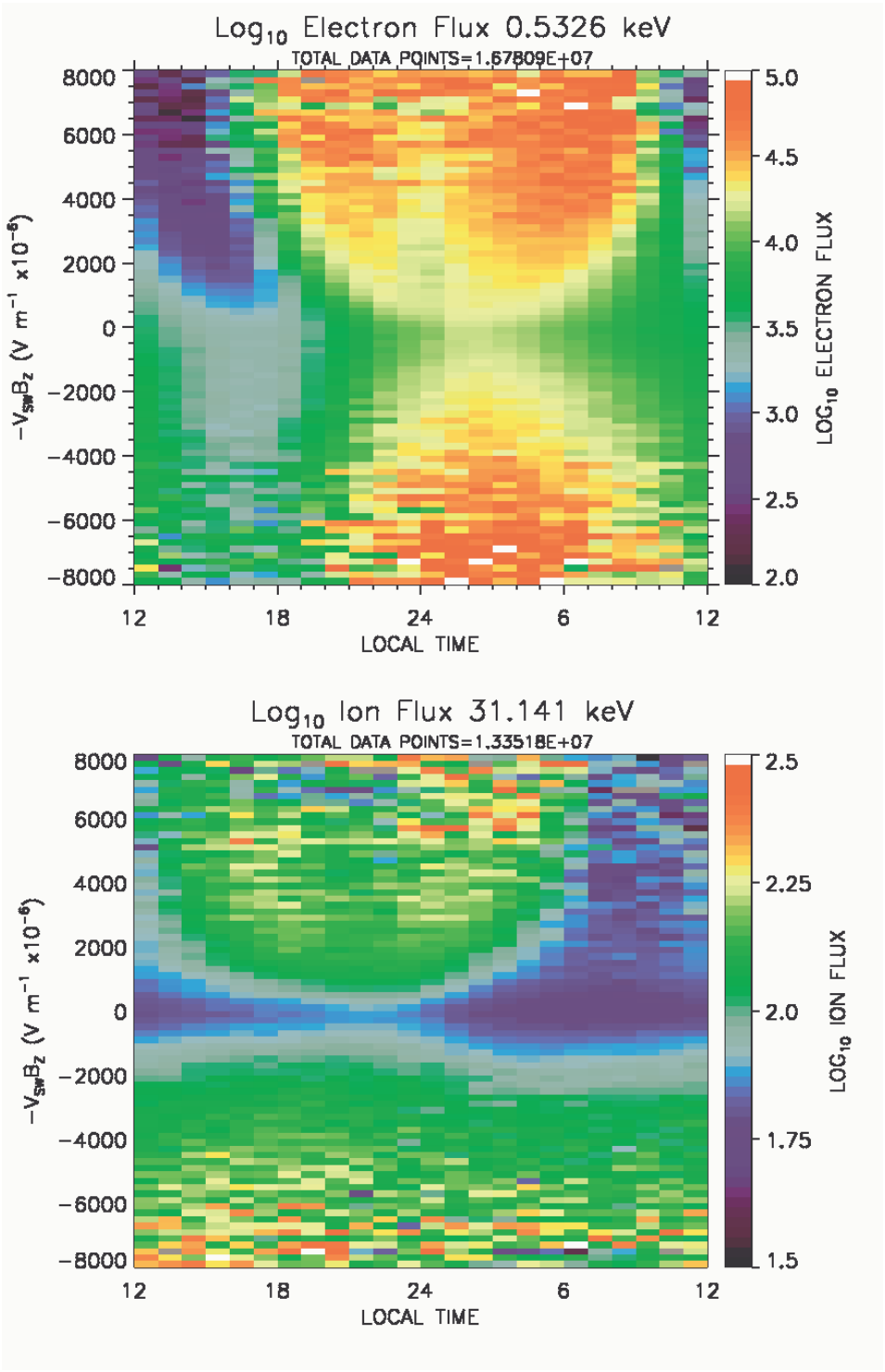

Figure 3. Example mean fluxes from LANL/MPA as a function of solar-wind electric field and local time, for the electrons (top panel - 532.6 eV) and the ions (bottom panel - 31141 eV). These plots demonstrate the large difference in the average flux at GEO for cases where the IMF is northwards (negative $-v_{sw}B_z$) or southwards (positive $-v_{sw}B_z$).

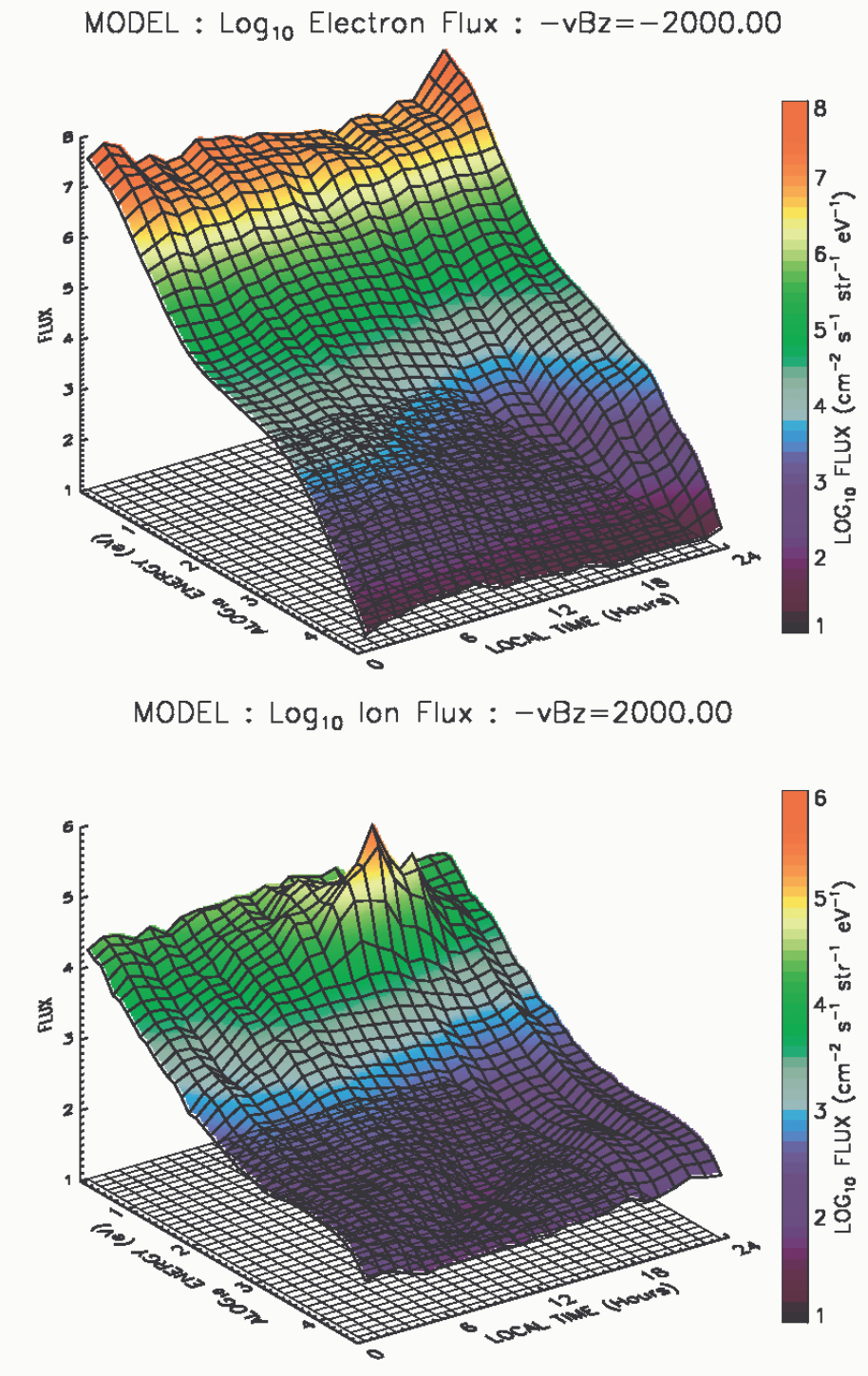

Figure 4. Example surfaces showing the model flux surfaces at two different values of $-v_{sw}B_z$, for electrons (top: $-vB_z = 2000$ μV m^{-1}.) and ions (bottom: $-vB_z = -2000$ μV m^{-1}.), as a function of energy and local time. Flux values at points off the grid can be computed via bi-linear interpolation between grid points, and subsequent linear interpolation between the discrete values of $-v_{sw}B_z$.

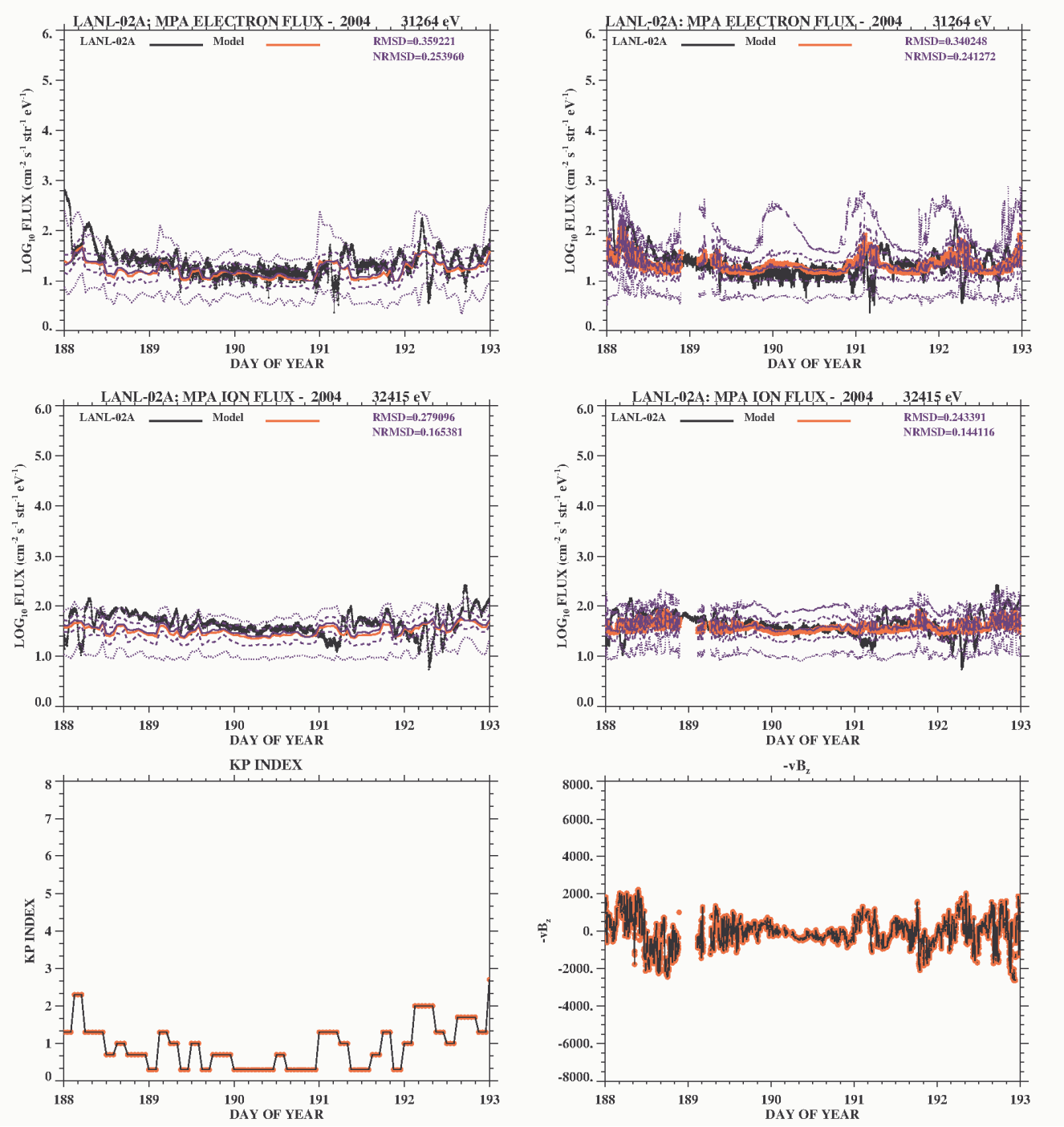

Figure 5. Example model results for five very calm days in 2004 for electrons and ions with energies ~32 keV. The left column shows the model predictions for electrons and ions using the Kp version of the model. The right column shows model predictions in the same format, but using the $-v_{sw}B_z$ version of the model. The black line shows the observations from the LANL-02A satellite. The solid red line is the predicted mean flux, and the solid purple line is the median. The 5th, 25th, 75th and 95th percentiles are indicated by the dashed and dotted purple lines. The Kp index and the $-v_{sw}B_z$ parameter are also shown in the bottom row.

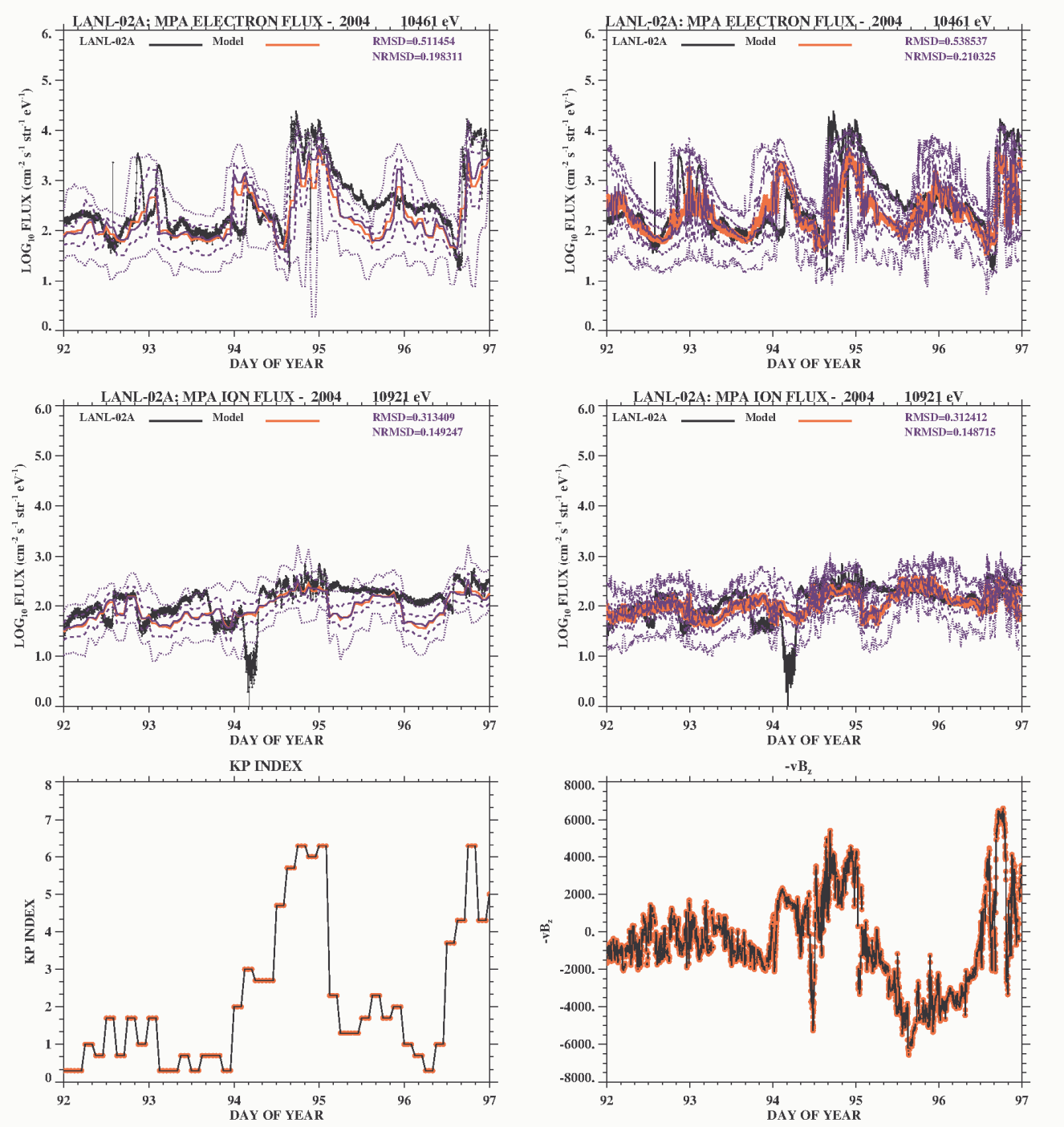

Figure 6. Example model results for five disturbed days in 2004 for electrons and ions with energies ~10 keV. The left column shows the model predictions for electrons and ions using the Kp version of the model. The right column shows model predictions in the same format, but using the $-v_{sw}B_z$ version of the model. The black like shows the observations from the LANL-02A satellite. The solid red line is the predicted mean flux, and the solid purple line is the median. The 5th, 25th, 75th and 95th percentiles are indicated by the dashed and dotted purple lines. The Kp index and the $-v_{sw}B_z$ parameter are also shown in the bottom row.

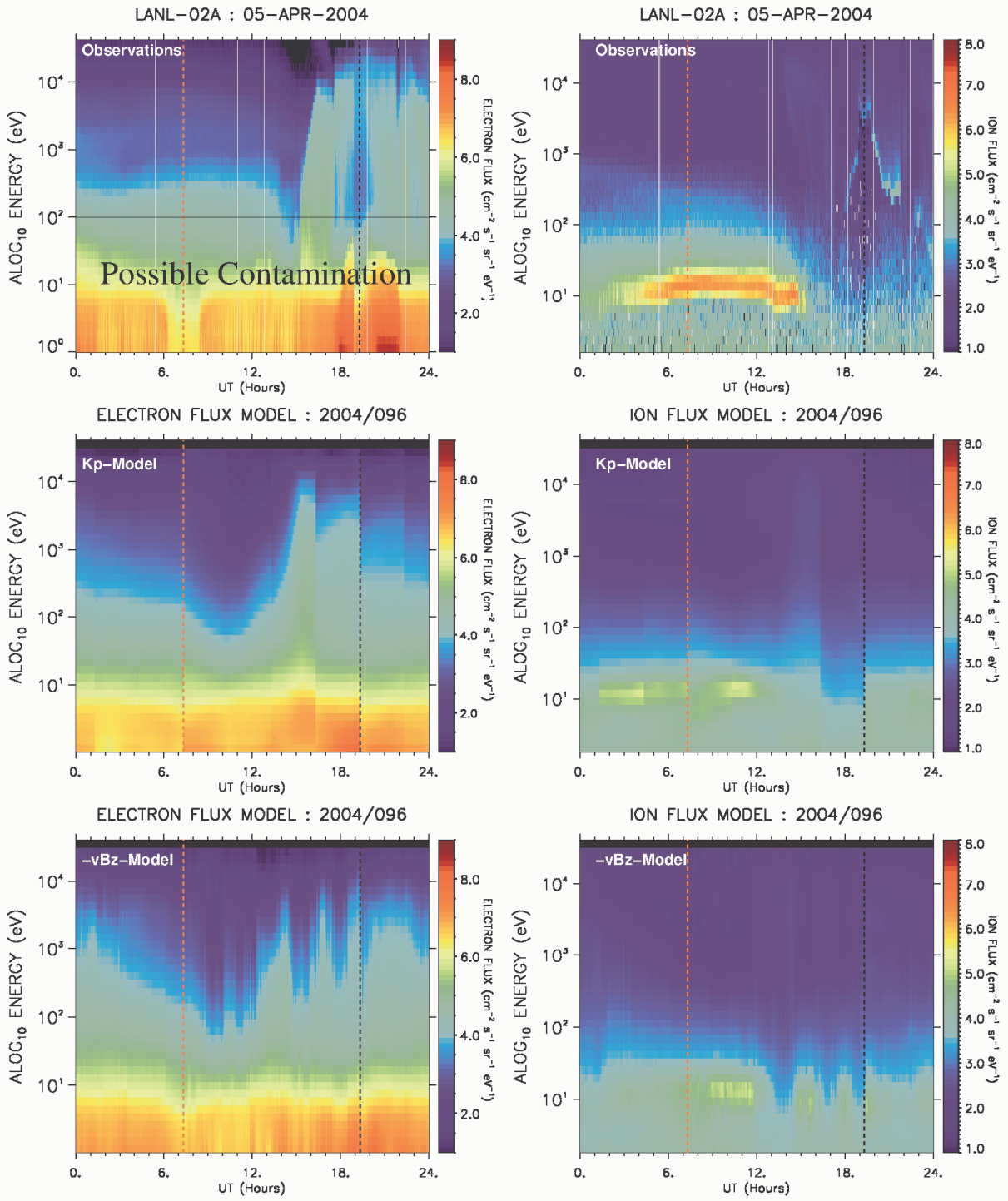

Figure 7. Comparison of particle flux observations (top row) with the Kp-model (middle row) and the new $-v_{sw}B_z$ model (bottom row) for electrons (left column) and ions (right column) on 5th April (day-of-year 96) in 2004. Large fluctuations occur in both the Kp index and in the $-v_{sw}B_z$ parameter on this day (see Figure 6). The orange line marks local noon and the black line marks local midnight in each plot.

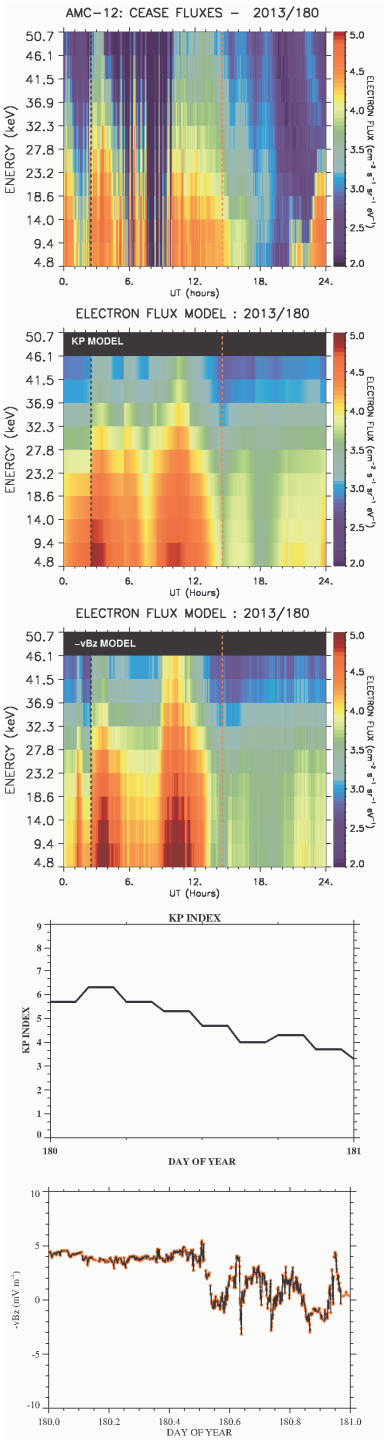

Figure 8. Figure showing the CEASE-II electron flux observations from AMC-12 (top panel) on 29th June (DOY- 180) in 2013 during disturbed geomagnetic activity. Also shown are the electron flux predictions from the Kp model (middle panel), and the electron flux predictions from the $-v_{sw}B_z$ model (bottom panel). Note: the CEASE-II electron fluxes have been multiplied by a constant factor (cross-calibrated) to bring them into alignment with the LANL/MPA model fluxes. Kp and $-v_{sw}B_z$ are also shown.

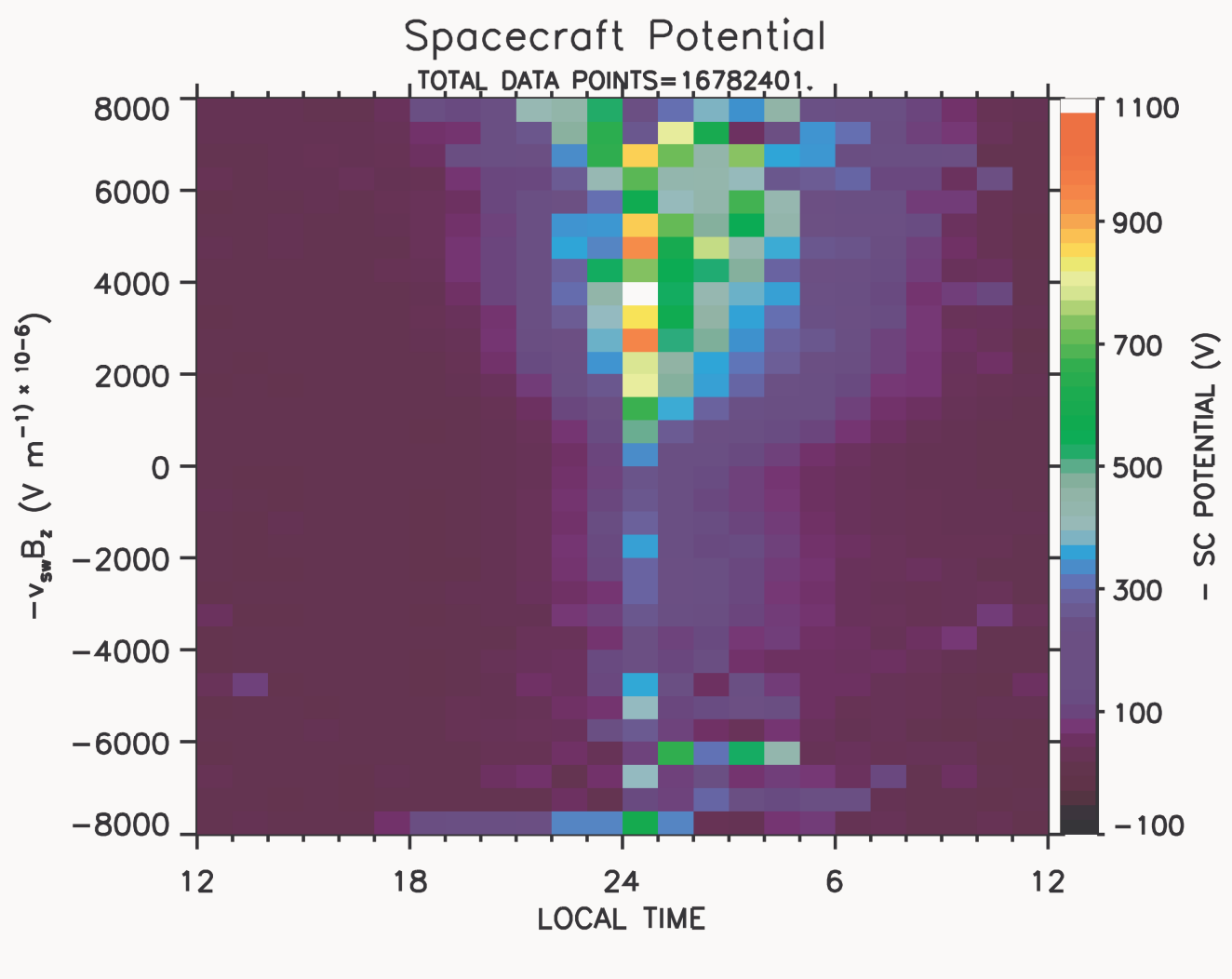

Figure 9. Showing the mean (negative) of the spacecraft potential measured by MPA spacecraft between 1990 and 2007 as a function of $-v_{sw}B_z$ and local time. The spacecraft surface potential is clearly most elevated around local midnight, and during southwards excursions of IMF-B_z.